Inorganic Chemistry

pubs.acs.org/IC Article

Crystal Growth of Quaternary $AkRE_2Si_2S_8$ (Ak = Ca and Sr; RE = La-Tb) Thiosilicates Using Flux-Assisted Boron Chalcogen Mixture Method: Exploring X-ray Scintillation, Luminescence, and Magnetic Properties

Gopabandhu Panigrahi, Anna A. Berseneva, Gregory Morrison, Adam A. King, Robin L. Conner, Luiz G. Jacobsohn, and Hans-Conrad zur Loye*



Cite This: Inorg. Chem. 2024, 63, 12849-12857



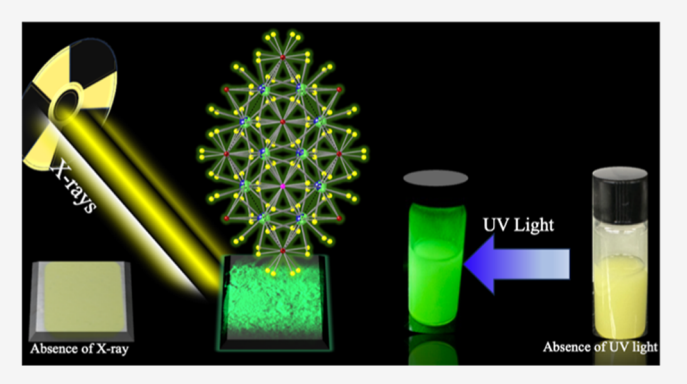
ACCESS |

III Metrics & More

Article Recommendations

Supporting Information

ABSTRACT: We report on the detailed structural analysis of a series of 11 new quaternary rare earths containing thiosilicates, $AkRE_2Si_2S_8$ (Ak = Ca and Sr; RE = La, Ce, Pr, Nd, Sm, Gd, and Tb), synthesized using the flux-assisted boron chalcogen mixture method. High quality crystals were grown and used to determine their crystal structures by single crystal X-ray diffraction. All members of the $AkRE_2Si_2S_8$ series crystallize in the trigonal crystal system with space group R3c (space group no. 167). Polycrystalline powders were used for physical property measurements, including magnetic susceptibility, diffuse reflectance in the UV—visible range, and scintillation. Magnetic measurements indicated that $CaRE_2Si_2S_8$ (RE = Nd and Tb) exhibits paramagnetic behavior with a slightly negative Weiss constant. The band gaps of the



materials were determined from diffuse reflectance data, and optical band gaps were estimated to be 2.5(1) and 2.9(1) eV for $CaCe_2Si_2S_8$ and $CaGd_2Si_2S_8$, respectively. $CaCe_2Si_2S_8$, $CaTb_2Si_2S_8$, and $SrCe_2Si_2S_8$ exhibited intense green luminescence upon irradiation with 375 nm ultraviolet light and, furthermore, scintillated when exposed to X-rays. Radioluminescence measurements of $CaCe_2Si_2S_8$ powder revealed green emission with an intensity approximately 14% of that emitted by bismuth germanium oxide powder.

■ INTRODUCTION

Complex metal chalcogenides are well-known for their structural diversity and extensive physical properties and, consequently, their synthesis has been widely explored. 1-5 As a class, chalcogenides are more polarizable than oxides and also exhibit a tendency to self-catenate, often leading to relatively complex structures that exhibit interesting electronic structures and functionalities. Lanthanide-containing chalcogenides, in particular, have garnered attention for their capacity to form intricate ternary and quaternary compounds, as have many main group and transition element-containing compositions. These novel structures of metal chalcogenides have paved the way for numerous applications, including thermoelectrics, photovoltaics, optics, optics, nonlinear optics, and scintillation.

Scintillators, essential for X-ray or γ -ray detection, hold significant importance for their widespread use in computed tomography scanners, for detecting radioactive contaminants, as well as for security and other medical and industrial applications. ^{16–20} Different approaches for the development of new luminescent and potentially scintillating materials include

the incorporation of luminophores into specific crystal structures. 21 In the past decades, many fluorescent sulfide materials were developed by doping select crystal structures with transition or rare earth elements, $^{22-24}$ where the dopant partially or fully occupies the crystallographic sites of a host material. For example, the partial doping of the quaternary thiosilicate $BaLa_2Si_2S_8$ with Ce^{3+} makes it suitable for potential LED applications. 25

Although these materials hold immense potential for various applications, their synthesis is challenging due to the high reactivity of rare earth metals toward moisture and air, as well as the unavailability of commercially available rare earth chalcogenides. The zur Loye group has addressed this issue by employing the boron chalcogen mixture (BCM) method,

Received: March 31, 2024 Revised: June 17, 2024 Accepted: June 21, 2024 Published: June 29, 2024





Table 1. Crystallographic Information of AkRE₂Si₂S₈ (Ak = Ca and Sr; RE = La, Ce, Pr, Nd, Sm, Gd, and Tb)

	chemical formula						
	CaLa ₂ Si ₂ S ₈	CaCe ₂ Si ₂ S ₈	CaPr ₂ Si ₂ S ₈	CaNd ₂ Si ₂ S ₈	CaSm ₂ Si ₂ S ₈	CaGd ₂ Si ₂ S ₈	
color	white	yellow	green	blue	yellow	off white	
formula weight	630.55	632.97	639.76	641.21	653.44	667.23	
space group	trigonal, $R\overline{3}c$						
temperature (K)	299 (2)	298 (2)	300 (2)	300 (2)	298 (2)	299 (2)	
a (Å) c (Å)	9.0138 (2), 26.643 (8)	8.9650 (1), 26.4740 (8)	8.9314 (1), 26.3402 (7)	8.9063 (2), 26.2446 (8)	8.8624 (1), 26.0418 (6)	8.8348 (1), 25.8964 (5)	
V (Å ³)	1874.74 (10)	1842.68 (7)	1819.65 (6)	1802.87 (10)	1771.35 (6)	1750.50 (5)	
density (mg/m³)	3.351	3.422	3.474	3.544	3.675	3.798	
abs coeff (mm ⁻¹)	8.63	9.24	9.88	10.51	11.84	13.29	
Z	6.0	6.0	6.0	6.0	6.0	6.0	
$R_{ m int}$	0.026	0.023	0.026	0.027	0.027	0.025	
R1, wR2	0.014, 0.037	0.015, 0.040	0.014, 0.035	0.016, 0.041	0.016, 0.038	0.019, 0.042	
GOF (F^2)	1.11	1.14	1.12	1.11	1.14	1.20	
$(\mathrm{e}^{\Delta ho_{\mathrm{max'}}}_{\mathrm{A}}^{\Delta ho_{\mathrm{min}}}$	0.88, -0.84	1.08, -0.83	1.21, -0.86	1.38, -0.98	1.69, -1.24	1.73, -1.34	
		chemical formula					
		CaTh C: C	CuT a C: C	CarCar C: C	C.D. C: C	C.MIJ C: C	

	chemical formula					
	CaTb ₂ Si ₂ S ₈	SrLa ₂ Si ₂ S ₈	SrCe ₂ Si ₂ S ₈	$SrPr_2Si_2S_8$	SrNd ₂ Si ₂ S ₈	
color	off white	white	yellow	green	blue	
formula weight	670.17	678.09	680.51	682.10	688.76	
space group	trigonal, $R\overline{3}c$					
temperature (K)	299 (2)	299 (2)	299 (2)	298 (2)	299 (2)	
a (Å)	8.8135 (2)	9.0723 (3)	9.0233 (2)	8.9965 (2)	8.9677 (2)	
c (Å)	25.7773 (3)	26.9412 (11)	26.7633 (7)	26.6515 (8)	26.5582 (8)	
V (Å ³)	1734.06 (8)	1920.36 (15)	1887.13 (10)	1868.10 (10)	1849.66 (10)	
density (mg/m³)	3.851	3.518	3.593	3.638	3.710	
abs coeff (mm ⁻¹)	14.16	12.15	12.81	13.45	14.10	
Z	6.0	6.0	6.0	6.0	6.0	
$R_{\rm int}$	0.042	0.028	0.031	0.031	0.049	
R1, wR2	0.037, 0.094	0.015, 0.036	0.022, 0.048	0.026, 0.054	0.026, 0.047	
GOF (F^2)	1.48	1.11	1.13	1.14	1.13	
$\Delta ho_{ m max}$ $\Delta ho_{ m min}$ (eÅ $^{-3}$)	1.08, -1.68	1.65, -1.37	2.32, -1.92	2.59, -2.22	2.15, -1.70	

which provides a straightforward route for synthesizing mixed metal chalcogenides starting from metal oxide precursors. Many lanthanides and actinides containing chalcogenides, including thiophosphates and thiosilicates, were previously reported synthesized using the BCM synthesis route.²⁶⁻² Despite the existence of several reported series of thiosilicates, there remains significant room for the exploration of additional structural families and compositions, which is made possible by the thiosilicates' extensive structural flexibility. 29-32 Recently, the zur Loye group reported on two series of quaternary thiosilicates (RE₃Mg_{0.5}SiS₇ and RE₃TM_{0.5}SiS₇), ^{26,33} a class of chalcometallates synthesized via the BCM method. During the synthesis of the RE₃Mg_{0.5}SiS₇ series, we observed the presence of a trace secondary phase, identified as CaCe₂Si₂S₈, where calcium originated from the flux used for crystal growth. This yellow, fluorescent compound crystallizes in the La₂PbSi₂S₈ crystal structure type.³¹

The intriguing characteristics exhibited by $CaCe_2Si_2S_8$ piqued our interest and prompted us to more extensively explore this family, as, to the best of our knowledge, only a small number (\sim 20 compounds) of its members have been reported in the ICSD database. ^{25,31,34} All of these compounds were synthesized through solid-state synthesis via sintering their elemental constituents in evacuated quartz tubes. In our exploration, we synthesized and comprehensively characterized a series of 11 new compositions belonging to the AkRE₂Si₂S₈ family (Ak = Ca and Sr; RE = La, Ce, Pr, Nd, Sm, Gd, and

Tb). The successful synthesis of both single crystal and polycrystalline phases provided us with the opportunity to thoroughly examine their physical properties. Herein, we present our findings on the crystal growth of high-quality single crystals of $AkRE_2Si_2S_8$ along with their single crystal structure determination, and furthermore, we report on our investigation of the optical, magnetic, thermogravimetric, and scintillation properties of selected compounds within this series.

EXPERIMENTAL SECTION

 $\rm RE_2O_3$ (RE = La, Nd, Sm, and Gd) (99.9%, Alfa Aesar), $\rm CeO_2$ (99.9%, Alfa Aesar), $\rm Pr_6O_{11}$ (99.9%, Alfa Aesar), $\rm Tb_4O_7$ (99.9%, Alfa Aesar), sulfur powder (99.5% Fisher scientific), boron (crystalline 100 mesh, 99.9%, Beantown Chemicals), $\rm SiO_2$ (amorphous powder, 99.9%, Alfa Aesar), NaCl (99.9%, Alfa Aesar), and CaCl $_2$ (Fisher Scientific). The CaCl $_2$ –NaCl eutectic mixture used for the synthesis was stored in a drying oven set to 260 °C to maintain the anhydrous state of the salts.

 $CaRE_2Si_2S_8$ (RE = La–Tb) single crystals were synthesized by the addition of 50 mg of RE_2O_3 (RE = La, Nd, Sm, and Gd), CeO_2 , Pr_6O_{11} , Tb_4O_7 , 20 mg of boron, 90 mg of sulfur, and 5 mg of SiO_2 powder into a heavily carbon-coated fused silica tube (12 mm outer diameter) along with 75 mg of the $CaCl_2$ –NaCl eutectic mixture. The fused silica tube was evacuated to 10^{-4} Torr and flame-sealed using a methane/oxygen torch. The sealed fused silica tube was placed into a programmable muffle furnace set to heat to 950 °C in 20 h, dwell at this temperature for 20 h, and cool to 750 °C in 20 h, at which point the furnace was shut off and allowed to cool down to room temperature. $SrRE_2Si_2S_8$ (RE = La–Nd) was synthesized using the

same synthesis procedure except that 75 mg of the SrCl₂–NaCl eutectic mixture was used instead of the CaCl₂–NaCl mixture.

To prepare larger quantities of samples for physical property measurements of $AkRE_2Si_2S_8$ (Ak = Ca and Sr) powders, the flux-assisted BCM method was used, and the reactant and flux quantities were both increased. The reactants were ground using a mortar and pestle, and the ground mixture was transferred to a carbon-coated fused silica tube. The sealed fused silica tubes containing reactants and flux were placed inside a programmable muffle furnace set to ramp to 950 $^{\circ}\text{C}$ in 20 h, dwell there for 20 h, and cool to 750 $^{\circ}\text{C}$ in 20 h, followed by shutting off the furnace and letting it cool down to room temperature.

The resulting product exhibited stability in air and moisture. It was washed three times with methanol and subjected to sonication to remove any remaining flux. The phase purity of the compounds was confirmed by powder X-ray diffraction analysis, and these samples were used for physical property measurements.

CAUTION

Boron sulfides are prone to moisture sensitivity, leading to the generation of H_2S gas upon contact with water or moisture. Therefore, all reaction procedures must be conducted within fume hoods, with strict adherence to safety protocols.

Single Crystal X-ray Diffraction (SCXRD). A Bruker D8 QUEST instrument equipped with a photon II mixed mode detector was used to collect room temperature SCXRD data sets of the AkRE₂Si₂S₈ series (Ak = Ca and Sr; RE = La, Ce, Pr, Nd, Sm, Gd, and Tb). An Incoatec microfocus X-ray source (Mo Kα radiation, λ = 0.71073 Å) was used for the diffraction experiment. Suitable size crystals were picked under immersion oil for unit cell determination. The working voltage and operating current were 50 kV and 1.4 mA, respectively, throughout the experiment. The detector to crystal distance of 40 mm was fixed, and an exposure time of 10 s/frame was used for the data collection. The raw area detector data frames were reduced and corrected for absorption using the SAINT+ and SADABS programs.³⁵

Final unit cell parameters were determined by least-squares refinement of large sets of reflections taken from each dataset.³⁶ An initial structural model was obtained with SHELXT. The XPREP program suggested rhombohedral symmetry with the R-centering of the unit cell and indicated possible space groups R3c (space group no. = 161) and R3c(space group no. = 167) consistent with the observed extinction conditions of the reflections. The statistical intensity $(|E_2-1|)$ value indicates a centrosymmetric structure for all of these crystals. Hence, the centrosymmetric trigonal R3c (no = 167) space group was used for the structure solution. Subsequent difference Fourier calculations and full-matrix least-squares refinement against F^2 were performed with SHELXL³⁷ using the Olex2 interface.³⁸ The PLATON's ADDSYM program agreed with the solved model and did not suggest any higher symmetric space group for the final structure.³⁹ All atoms were refined with anisotropic displacement parameters. The asymmetric unit contains four independent crystallographic atomic positions, with RE and Ak (Ak = Ca and Sr) exhibiting antisite mixing, both being present on the same sites (18e). The mixed metal sites have occupancies of 1/3 Ak atoms and 2/3 RE atoms. The structure contains one Si atom (12c) and two S atoms [S1 (12c) and S2 (36f)]. Crystallographic and refinement data pertinent to all of the title compounds are provided in Table 1.

Powder X-ray Diffraction (PXRD). PXRD data were obtained by analyzing finely ground powder samples of

AkRE $_2$ Si $_2$ S $_8$ prepared using the molten flux synthesis method. PXRD data were collected on a Bruker D2 PHASER diffractometer using Cu–K $_{\alpha}$ radiation (λ = 1.5418 Å) over the 2 θ range 5–65° with a step size of 0.02°.

Energy-Dispersive X-ray Spectroscopy (EDS). EDS data were collected on single crystals by mounting them directly onto a SEM stub using conducting carbon tape. Quantitative elemental analysis was performed utilizing a Tescan Vega-3 SEM instrument, which was fitted with a Thermo EDS attachment. The SEM operated in a low-vacuum mode with a 15–20 kV accelerating voltage and a 40 s accumulation time. The summarized SEM results can be found in the Supporting Information.

Thermogravimetric Analysis (TGA). TGA was conducted on polycrystalline powder samples by utilizing an SDT Q600 thermogravimetric analyzer. An alumina pan served as the sample holder. The samples were heated from room temperature to 500 °C at a rate of 5 °C/min under varying gaseous environments (nitrogen gas and air) with a controlled flow rate of 100 mL/min. Subsequently, the resulting powders were further analyzed by PXRD for phase identification.

UV-visible Spectroscopy. UV-visible reflectance spectra were recorded using a PerkinElmer lambda 35 UV-vis spectrophotometer. The spectrophotometer was operated in diffuse reflectance mode and was equipped with an integrating sphere. Reflectance data were converted internally to absorbance data via the Kubelka-Munk function. Spectra were recorded over the 250–900 nm range at room temperature and ambient conditions on powder samples.⁴⁰

Photoluminescence. Microphotoluminescence data were collected using a HORIBA scientific standard microscope spectroscopy system, which was outfitted with a HORIBA iHR320 imaging spectrograph and a sincerity CCD detector. A confocal 375 nm diode laser served as the excitation source. Data were acquired by utilizing Labspec 6 within the 400–800 nm range, employing a laser excitation source power of 10.0 mW and a 10× UV objective.

Scintillation. Radioluminescence (RL) measurements were carried out using a customer-designed configuration of the Freiberg Instruments Lexsyg spectrofluorometer equipped with a varian medical systems VF-50j X-ray tube with a tungsten target. The X-ray source was coupled with a crystal photonics CXD-S10 photodiode for continuous radiation intensity monitoring. For RL measurements, the light emitted by the sample was collected by an Andor Technology SR-OPT-8024 optical fiber connected to an Andor Technology Shamrock 163 spectrograph coupled to a cooled (-80 °C) Andor Technology DU920P-BU Newton CCD camera (spectral resolution of ~0.5 nm/pixel). RL was measured under continuous X-ray irradiation (W lines and bremsstrahlung radiation; 40 kV, 1 mA) with an integration time of 10 s. The powdered glass samples filled ~8 mm diameter and 0.5 mm deep cups, thus allowing for comparison and the determination of relative RL luminosity against bismuth germanium oxide (BGO) powder [Alfa Aesar Puratronic, 99.9995% (metals basis)]. Relative luminosity results correspond to the ratio of the spectra integral from 300 to 750 nm, using the BGO spectrum integral as a reference. RL as a function of the temperature was executed with a 1 °C/s heating rate, 5 s integration time, and a 5 s interval between two consecutive acquisitions such that each spectrum was accumulated within a 5 °C interval every 10 °C from room temperature to 300 °C. These spectra were labeled by the starting acquisition

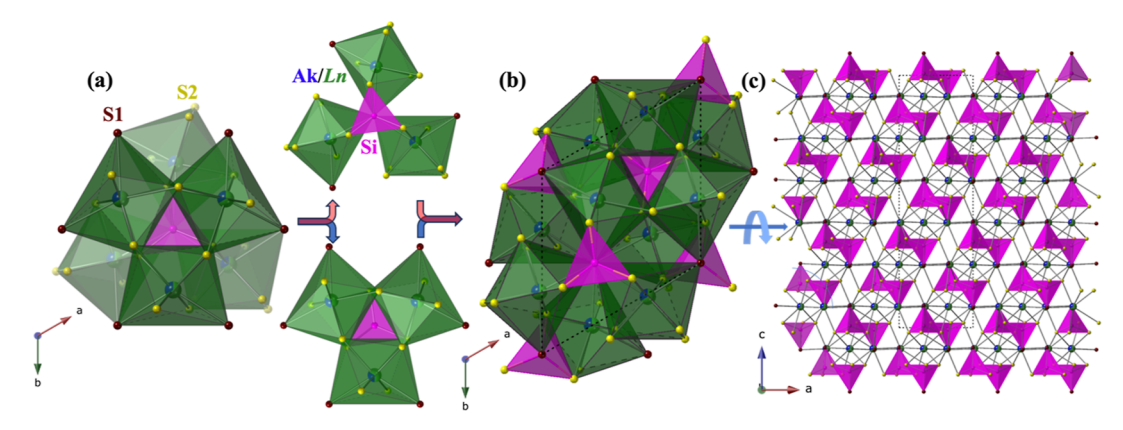


Figure 1. (a) Repeating unit, (b) unit cell representation of $AkRE_2Si_2S_8$ along c-direction, and (c) b-direction.

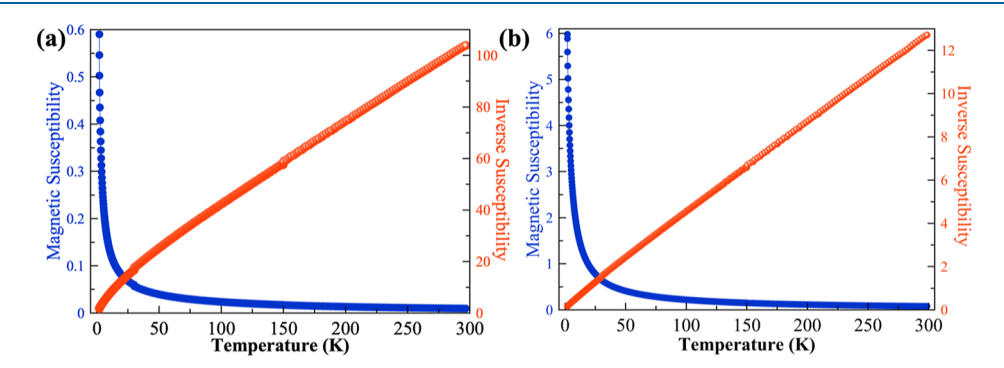


Figure 2. Molar susceptibility and inverse molar susceptibility vs temperature plots for polycrystalline (a) CaNd₂Si₂S₈ (left) and (b) CaTb₂Si₂S₈ (right) measured in an applied field of 1000 Oe.

temperature. All RL spectra were automatically corrected by using the spectral response of the system determined by the manufacturer.

RESULTS AND DISCUSSION

Synthesis. The presence of a trace secondary phase, identified as CaCe₂Si₂S₈, was observed after the synthesis of the RE₃Mg_{0.5}SiS₇ series. Building on this observation, the synthesis of this composition was extended to additional compositions using the BCM method. The RE₂O₃ and SiO₂ oxide reagents served as rare earth and silicon sources, and boron was used to remove oxygen from the oxide reagents, thus leaving these elements available for reacting with elemental sulfur to form the chalcogenides. In this synthesis, the eutectic CaCl₂/NaCl flux functioned both as a flux and as a source of calcium. We successfully synthesized seven new compounds within the $CaRE_2Si_2S_8$ series (RE = La, Ce, Pr, Nd, Sm, Gd, and Tb) by varying the lanthanide RE₂O₃ reagent from RE = La to Tb. EDS elemental analyses confirmed the presence of all expected elements in the crystals (refer to Figure S1a,e and Table S1-S7) and confirmed the absence of any extraneous elements. Despite our efforts to incorporate the smaller lanthanides, we were unable to obtain compositions containing rare earth elements smaller than terbium, including europium. We suspect that the terbium-containing composition, CaTb₂Si₂S₈, represents the size limit for the lanthanides in the calcium series. The fact that Eu prefers the +2 oxidation state in chalcogenides is the likely reason for our inability to obtain this composition. To target additional compositions, we explored the substitution of Sr for Ca, which enabled us to synthesize four new Sr-based quaternary thiosilicates, $SrRE_2Si_2S_8$ (RE = La-Nd). The Sr for Ca substitution was

accomplished by changing the flux from $CaCl_2/NaCl$ to $SrCl_2/NaCl$

For both series, the reaction products were washed with methanol to dissolve the flux and remove impurities, resulting in phase-pure samples (Figure S2–S12). This also allowed us to determine that these phases are stable to ambient conditions. EDS elemental analysis of SrRE₂Si₂S₈ (RE = Ce and Nd) confirmed the presence of all expected elements in the crystals (see Figure S1f,g) and confirmed the absence of any extraneous elements. The thermal stability of CaRE₂Si₂S₈ (RE = Ce and Tb) polycrystalline powder samples was evaluated via TGA in atmospheres of either flowing air or nitrogen up to a temperature of 500 °C. PXRD analyses of the post TGA samples confirmed the thermal stability of these phases up to 500 °C (see Figure S13–S17).

Crystal Structure. The compounds $AkRE_2Si_2S_8$ crystallize in the $R\overline{3}c$ space group, and are isostructural with the previously reported lead-based series, $R_2PbSi_2S_8$ (R=Y, Ce, Pr, Nd, Sm, Gd, Tb, Dy, and Ho) and $BaLa_2Si_2S_8$. The unit cell contains four independent atomic sites, with the metal site 18e being randomly occupied by both rare earth and alkaline earth cations. For each composition, the occupancy factor of the 18e metal site was refined, resulting in a numerical value close to 2/3 RE + 1/3 Ak, aligning well with the expected ratio based on the charge balance. Consequently, the mixed metal site occupancies were fixed as 2/3 RE + 1/3 Ak in all $AkRE_2Si_2S_8$ compounds throughout the final refinement process. The crystal data and refinement details are summarized in Table 1.

The unit cell structure along the *c*-direction is shown in Figure 1b, where the three-dimensional structure is formed by edge- and corner-sharing of neighboring $(1/2 \text{ RE} + 1/3 \text{ Ak})S_8$

bicapped trigonal prisms and $SiS(1)S(2)_3$ tetrahedral units. Figure 1a depicts the repeating unit of the structure, which consists of six $(1/2 \text{ RE} + 1/3 \text{ Ak})S_8$ and one $SiS(1)S(2)_3$ units. The edge- and corner-sharing $(1/2 \text{ RE} + 1/3 \text{ Ak})S_8$ bicapped trigonal prisms create tetrahedral cavities in which the silicon cations are located.

The RE–S bonds in the bicapped trigonal prisms range from 3.263(1) to 2.748(1) Å for the La to Tb compositions. The SiS_4 tetrahedra are irregular and have Si-S bonds ranging from 2.113(1) to 2.111(1) Å in the $CaRE_2Si_2S_8$ series. The corresponding bonds in the $SrRE_2Si_2S_8$ series range from 3.280(1) to 2.831(1) Å and 2.116(1) to 2.114(1) Å for the RE–S and Si–S distances, respectively (see Table S8). These bond lengths are consistent with those found in related chalcogenides. $^{33,41-44}$

Magnetic Properties. The temperature-dependent magnetization studies on polycrystalline samples of $CaRE_2Si_2S_8$ (RE = Nd and Tb) were carried out over the temperature range 2–300 K. The magnetic susceptibility (χ) was found to follow the Curie law on cooling to 2 K with no evidence of long-range magnetic ordering. The magnetic susceptibility vs temperature plots for $CaRE_2Si_2S_8$ (RE = Nd and Tb) are shown in Figure 2a,b. The inverse susceptibility data were fitted to the Curie law using the high temperature region (200–300 K) to calculate the Curie (C) and Weiss (θ) constants; the results are summarized in Table 2.

Table 2. Summary of the Magnetic Data for CaRE₂Si₂S₈ (RE = Nd and Tb)

compound	μ eff (per formula unit) from CW fit (200–300 K)	μ cal (per formula unit)	$\theta_{\rm W}$ (K)
CaNd ₂ Si ₂ S ₈	5.11	5.12	-44
$CaTb_2Si_2S_8\\$	14.06	13.75	-15

The effective magnetic moments determined from the linear fit are $5.11~\mu_{\rm B}$ per formula unit and $14.06~\mu_{\rm B}$ per formula unit, for the Nd and Tb compositions, respectively, which are in good agreement with those expected for Nd and Tb ions, 5.12 and $13.75~\mu_{\rm B}$, respectively. The negative Weiss constants observed for both compounds indicate antiferromagnetic interactions between f-electrons on neighboring rare-earth ions. No difference between the field-cooled (FC) and zero field-cooled (ZFC) data for either composition was observed; therefore, only the FC data is shown in Figure 2 (see Figure S18 for ZFC data). The M vs H plots measured at 2 K for both

compositions are indicative of the saturation magnetic moments with increasing magnetic fields (Figure 3a,b).

UV–visible Diffuse Reflectance Spectroscopy. The optical properties of the quaternary compounds $CaRE_2Si_2S_8$ (RE = Ce, Gd) were examined using polycrystalline powders. As expected, many weak absorption peaks were observed due to the f—f electronic transitions of the RE³⁺ cation. The Kubelka–Monk equation was employed to analyze the optical absorption data, as shown in Figure 4a,b. The absorption plots are consistent with band gaps of 2.5(1) eV ($CaCe_2Si_2S_8$) and 2.9(1) eV ($CaGd_2Si_2S_8$), indicating the semiconducting nature of the studied thiosilicates. The inset indicates the color of the polycrystalline $CaCe_2Si_2S_8$ (yellow) and $CaGd_2Si_2S_8$ (white) samples imaged using an optical microscope, in agreement with the observed band gaps.

Photoluminescence. Photoluminescence spectra were collected on individual single crystals of $CaCe_2Si_2S_8$, $SrCe_2Si_2S_8$, and $CaTb_2Si_2S_8$. All spectra were collected using an ultraviolet 375 nm diode laser as the excitation. The Cecontaining compounds, $AkCe_2Si_2S_8$, exhibit strong green luminescence, while $CaTb_2Si_2S_8$ exhibits a light green color. For $AkCe_2Si_2S_8$, a broad band emission spectrum was observed at \sim 525 nm, which is likely due to the 5d–4f electronic transition of the Ce^{3+} ion (Figure 5a). However, the shape of the emission band was strongly affected by self-absorption since the band gap of $CaCe_2Si_2S_8$ was determined to be 2.5(1) eV, leading to a cutoff around 500 nm. A similar rationale was expected to be applicable to $SrCe_2Si_2S_8$.

The CaTb₂Si₂S₈ compound exhibited multiple emission peaks at different energy levels (Figure 5b). Four strong emission peaks are observed at 485, 548, 582, and 612 nm, due to Tb³⁺ electronic transitions $^5D_4 \rightarrow ^7F_6$, $^5D_4 \rightarrow ^7F_5$, $^5D_4 \rightarrow ^7F_4$, and $^5D_4 \rightarrow ^7F_3$, respectively. The most intense peak is observed at 548 nm (green region), which is in good agreement with previously reported results. He-50

Scintillation of AkRE₂Si₂S₈ (Ak = Ca and Sr; and RE = Ce and Tb). We were motivated to investigate the possible existence of scintillation in CaCe₂Si₂S₈, SrCe₂Si₂S₈, and CaTb₂Si₂S₈ after confirming their photoluminescent properties. Crystals of CaCe₂Si₂S₈, SrCe₂Si₂S₈, and CaTb₂Si₂S₈ were irradiated by X-rays inside a Rigaku Ultima IV diffractometer equipped with a copper K_{α} X-ray source (λ = 1.54018) while visually monitoring its emission using a digital camera. All three compounds displayed bright green scintillation, with CaCe₂Si₂S₈ exhibiting the highest intensity among them (see Figure 6)

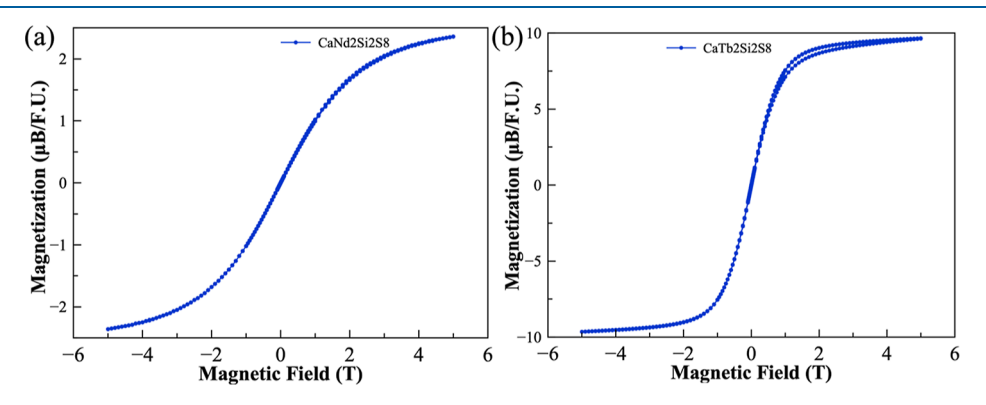


Figure 3. Magnetization as a function of applied field plots for polycrystalline (a) CaNd₂Si₂S₈ (left) and (b) CaTb₂Si₂S₈ (right) measured at 2 K.

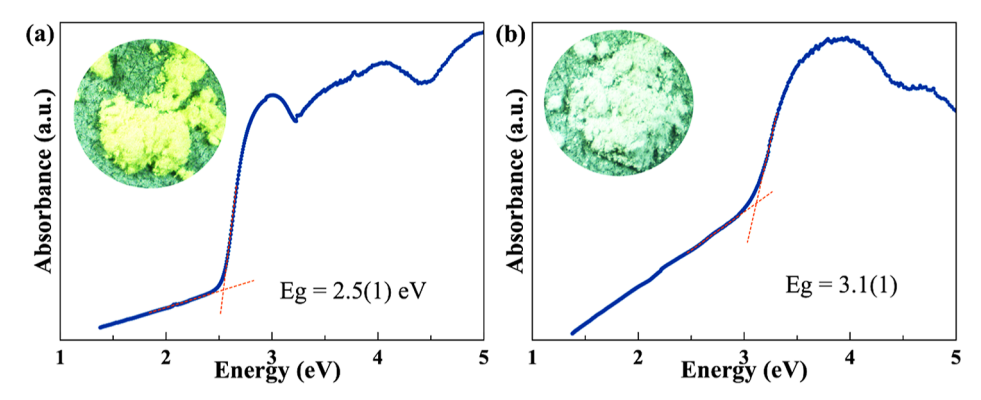


Figure 4. Optical absorption plot of polycrystalline (a) $CaCe_2Si_2S_8$ and (b) $CaGd_2Si_2S_8$ sample (inset figure shows the color of the corresponding compound).

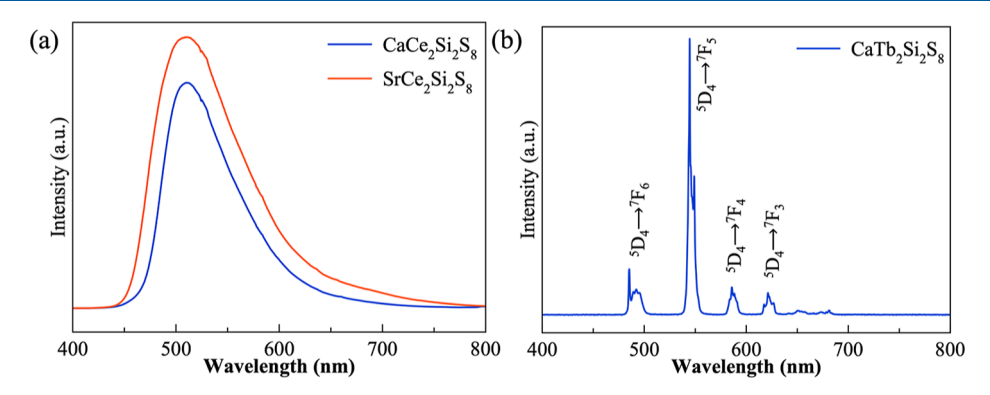


Figure 5. Emission spectra of (a) CaCe₂Si₂S₈ and SrCe₂Si₂S₈ and (b) CaTb₂Si₂S₈ crystals at room temperature under 375 nm excitation.

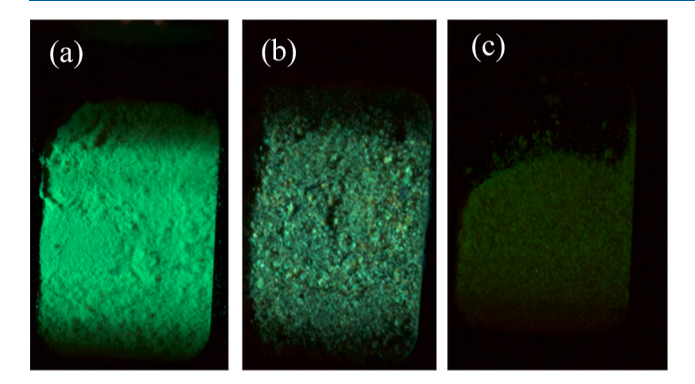


Figure 6. Scintillation of (a) CaCe₂Si₂S₈, (b) SrCe₂Si₂S₈, and (c) CaTb₂Si₂S₈ under Cu K_{α} X-ray irradiation.

The RL spectra of CaCe₂Si₂S₈, SrCe₂Si₂S₈, and CaTb₂Si₂S₈ powders were collected by using a dedicated spectrofluorometer (Figure 7a). CaCe₂Si₂S₈ and SrCe₂Si₂S₈, each produced a scintillation band centered at ~525 nm and CaTb₂Si₂S₈ produced scintillation with the same emission bands related to Tb³⁺, as reported above (Figure 5b). The integral emission of $CaCe_2Si_2S_8$, the brightest material, was compared with that of the commercial scintillator BGO, yielding a relative luminosity of 14% at room temperature (Figure 7b). Scintillation intensity is determined by the number of X-rays absorbed by the scintillator multiplied by the number of UV-visible light photons generated by each absorbed X-ray. The efficiency of this process depends on the conversion efficiency of generating electron-hole pairs by the X-rays, the transport efficiency of the charge carriers through the structure of the scintillator, and the efficiency of the

luminescence center, i.e., the rare earths Ce³⁺ and Tb³⁺. In addition, the material's transparency to its own emission, in part determined by its band gap, plays a major role in the final number of photons reaching the photodetector. While it is possible to calculate the X-ray mass attenuation coefficient of the compounds, where CaCe₂SiS₈ has the lowest coefficient among the ones investigated by RL in this work, the other quantities are not known. This situation hinders a deeper understanding of the causes of RL output. Still, further investigation into scintillation thermal quenching was conducted using the CaCe₂Si₂S₈ compound (Figure 8a) through high temperature RL measurements. Thermal quenching of CaCe₂Si₂S₈ scintillation was observed for higher temperatures, with emission completely quenched at approximately 293 °C. Overall, the peak position of the CaCe₂Si₂S₈ scintillation peak shifted to higher wavelengths with increasing temperature (Figure 8b). The peak intensity of the RL as a function of temperature was fitted using the Mott–Seitz model for thermal quenching (Figure 8c).⁵¹ This analysis yielded an estimated activation energy for nonradiative recombination of 0.24 eV, similar to the 0.37 eV value measured for Ce^{3+} in $Ba(La_{0.94}Ce_{0.06})_2Si_2S_8^{\ 25}$ with the caveat that transport losses of the scintillation process are incorporated in this thermal quenching analysis.

CONCLUSIONS

The modified flux-assisted BCM method offers a robust approach for the growth of high-quality quaternary thiosilicate crystals. A set of 11 new quaternary thiosilicates, $AkRE_2Si_2S_8$ (Ak = Ca and Sr; RE = La, Ce, Pr, Nd, Sm, Gd, and Tb), were synthesized utilizing a combination of molten flux and BCM approaches, resulting in both single crystals and polycrystalline

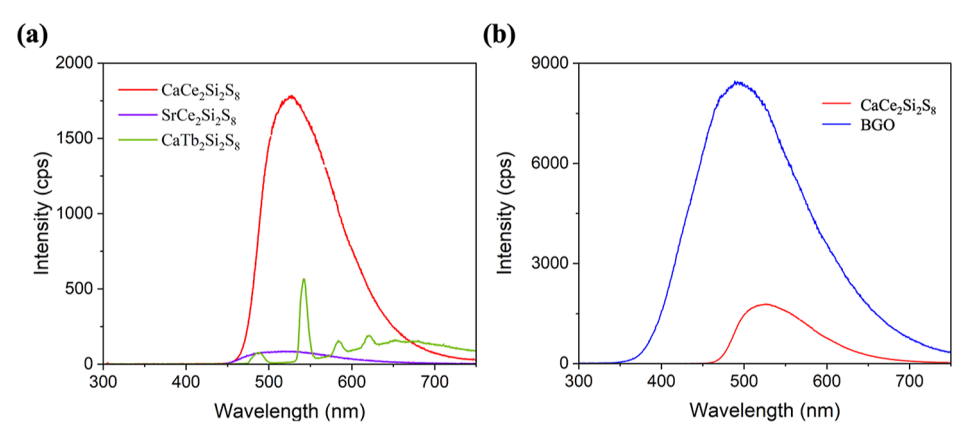


Figure 7. Radioluminescence spectra of (a) $CaCe_2Si_2S_8$ (red), $SrCe_2Si_2S_8$ (violet), and $CaTb_2Si_2S_8$ (green), and (b) comparison of the radioluminescence spectra of BGO (blue) and $CaCe_2Si_2S_8$ (red).

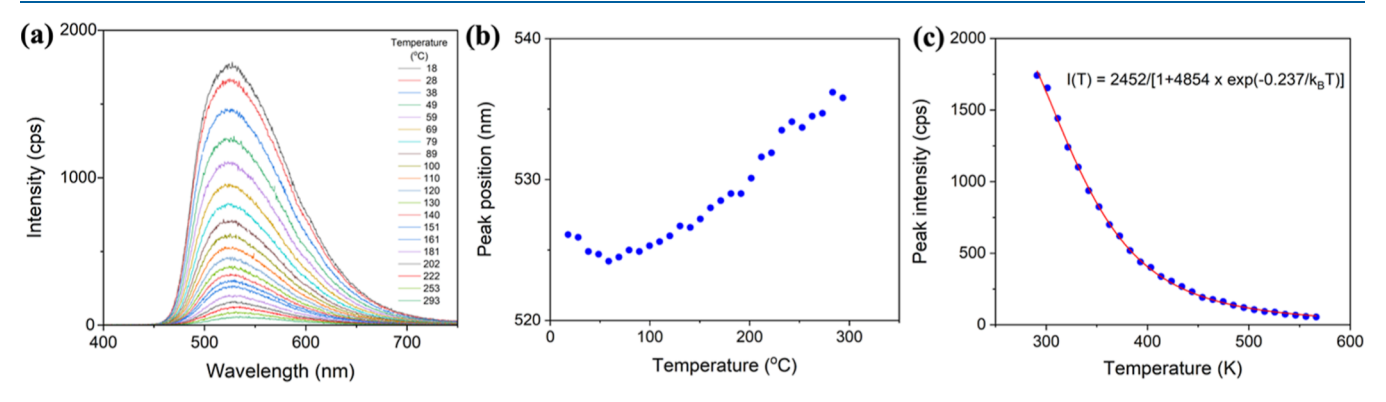


Figure 8. (a) RL spectra of CaCe₂Si₂S₈ as a function of the temperature. (b) Peak position of CaCe₂Si₂S₈ with respect to temperature, and (c) radioluminescence peak intensity of CaCe₂Si₂S₈ as a function of temperature. Peak intensity was fitted with the Mott–Seitz model (red line).

powders. These compounds exhibit a trigonal crystal structure in space group $R\overline{3}c$. The structures were determined by single crystal X-ray diffraction. Phase-pure polycrystalline materials were obtained and used for the subsequent investigation of the magnetic, luminescence, and scintillation properties. Moreover, the semiconducting nature of these materials was confirmed by UV-visible spectroscopy. CaCe₂Si₂S₈, SrCe₂Si₂S₈, and CaTb₂Si₂S₈ exhibited intense luminescence and also scintillation. The ability of this structure type to accommodate various elements suggests the potential for future expansion of this structural family. Exploring the substitution of Ge for Si holds promise for modifying specific properties, such as band gaps and scintillation, among others, which will be the focus of future studies. Additionally, the replacement of lanthanides with actinides presents a promising avenue for developing novel actinide materials. For all future studies, it is expected that the syntheses will be made possible by utilizing the BCM method.

ASSOCIATED CONTENT

Supporting Information

The Supporting Information is available free of charge at https://pubs.acs.org/doi/10.1021/acs.inorgchem.4c01314.

EDS results, TGA plots, and PXRD patterns of title compounds (PDF)

Accession Codes

CCDC 2336895-2336905 contain the supplementary crystallographic data for this paper. These data can be obtained free of charge via www.ccdc.cam.ac.uk/data request/cif, or by

emailing data_request@ccdc.cam.ac.uk, or by contacting The Cambridge Crystallographic Data Centre, 12 Union Road, Cambridge CB2 1EZ, UK; fax: +44 1223 336033.

AUTHOR INFORMATION

Corresponding Author

Hans-Conrad zur Loye — Department of Chemistry and Biochemistry, University of South Carolina, Columbia, South Carolina 29208, United States; orcid.org/0000-0001-7351-9098; Email: zurloye@mailbox.sc.edu

Authors

Gopabandhu Panigrahi – Department of Chemistry and Biochemistry, University of South Carolina, Columbia, South Carolina 29208, United States

Anna A. Berseneva — Department of Chemistry and Biochemistry, University of South Carolina, Columbia, South Carolina 29208, United States; orcid.org/0000-0002-1236-9329

Gregory Morrison – Department of Chemistry and Biochemistry, University of South Carolina, Columbia, South Carolina 29208, United States; ⊙ orcid.org/0000-0001-9674-9224

Adam A. King – Department of Chemistry and Biochemistry, University of South Carolina, Columbia, South Carolina 29208, United States

Robin L. Conner – Department of Materials Science and Engineering, Clemson University, Clemson, South Carolina 29634, United States

Luiz G. Jacobsohn – Department of Materials Science and Engineering, Clemson University, Clemson, South Carolina 29634, United States

Complete contact information is available at: https://pubs.acs.org/10.1021/acs.inorgchem.4c01314

Notes

The authors declare no competing financial interest.

ACKNOWLEDGMENTS

The authors gratefully acknowledge the support from the U.S. Department of Energy, Office of Basic Energy Sciences, Division of Materials Sciences and Engineering, under award DE-SC0018739. Synthesis, structural characterization, optical, and magnetic studies were conducted at the University of South Carolina. The work by R.L. Conner and L.G. Jacobsohn was supported by the NSF under grant no. DMR-1653016. RL measurements were performed at Clemson University.

REFERENCES

- (1) Gan, Y.; Miao, N.; Lan, P.; Zhou, J.; Elliott, S. R.; Sun, Z. Robust Design of High-Performance Optoelectronic Chalcogenide Crystals from High-Throughput Computation. *J. Am. Chem. Soc.* **2022**, *144* (13), 5878–5886.
- (2) Messegee, Z. T.; Cho, J. S.; Craig, A. J.; Garlea, V. O.; Xin, Y.; Kang, C.-J.; Proffen, T. E.; Bhandari, H.; Kelly, J. C.; Ghimire, N. J.; Aitken, J. A.; Jang, J. I.; Tan, X. Multifunctional Cu₂TSiS₄ (T = Mn and Fe): Polar Semiconducting Antiferromagnets with Nonlinear Optical Properties. *Inorg. Chem.* **2023**, *62* (1), 530–542.
- (3) Yuhas, B. D.; Smeigh, A. L.; Samuel, A. P. S.; Shim, Y.; Bag, S.; Douvalis, A. P.; Wasielewski, M. R.; Kanatzidis, M. G. Biomimetic Multifunctional Porous Chalcogels as Solar Fuel Catalysts. *J. Am. Chem. Soc.* **2011**, *133* (19), 7252–7255.
- (4) Berseneva, A. A.; zur Loye, H.-C. Advances in Chalcogenide Crystal Growth: Flux and Solution Syntheses, and Approaches for Postsynthetic Modifications. *Cryst. Growth Des.* **2023**, 23 (8), 5368–5383.
- (5) Berseneva, A. A.; Klepov, V. V.; Pal, K.; Seeley, K.; Koury, D.; Schaeperkoetter, J.; Wright, J. T.; Misture, S. T.; Kanatzidis, M. G.; Wolverton, C.; Gelis, A. V.; zur Loye, H.-C. Transuranium Sulfide via the Boron Chalcogen Mixture Method and Reversible Water Uptake in the NaCuTS₃ Family. *J. Am. Chem. Soc.* **2022**, *144* (30), 13773–13786.
- (6) Ishtiyak, M.; Panigrahi, G.; Jana, S.; Prakash, J.; Mesbah, A.; Malliakas, C. D.; Lebègue, S.; Ibers, J. A. Modulated Linear Tellurium Chains in Ba₃ScTe₅: Synthesis, Crystal Structure, Optical and Resistivity Studies, and Electronic Structure. *Inorg. Chem.* **2020**, *59* (4), 2434–2442.
- (7) Vogel, L.; Wonner, P.; Huber, S. M. Chalcogen Bonding: An Overview. *Angew. Chem., Int. Ed.* **2019**, *58* (7), 1880–1891.
- (8) Yu, Y.; Cagnoni, M.; Cojocaru-Mirédin, O.; Wuttig, M. Chalcogenide Thermoelectrics Empowered by an Unconventional Bonding Mechanism. *Adv. Funct. Mater.* **2020**, *30* (8), 1904862.
- (9) Fabini, D. H.; Koerner, M.; Seshadri, R. Candidate Inorganic Photovoltaic Materials from Electronic Structure-Based Optical Absorption and Charge Transport Proxies. *Chem. Mater.* **2019**, *31* (5), 1561–1574.
- (10) Gao, L.; Yang, Y.; Zhang, B.; Wu, X.; Wu, K. Triclinic Layered $A_2ZnSi_3S_8$ (A = Rb and Cs) with Large Optical Anisotropy and Systematic Research on the Inherent Structure-Performance Relationship in the $A_2MIIBMIV_3Q_8$ Family. *Inorg. Chem.* **2021**, *60* (16), 12573–12579.
- (11) Mishra, N.; Vasavi Dutt, V. G.; Arciniegas, M. P. Recent Progress on Metal Chalcogenide Semiconductor Tetrapod-Shaped Colloidal Nanocrystals and Their Applications in Optoelectronics. *Chem. Mater.* **2019**, 31 (22), 9216–9242.

- (12) Panigrahi, G.; Yadav, S.; Jana, S.; Ramanujachary, K. V.; Niranjan, M. K.; Prakash, J. Ba 4 FeAgS 6: A New Antiferromagnetic and Semiconducting Quaternary Sulfide. *Dalton Trans.* **2023**, *52* (3), 621–634.
- (13) Mumbaraddi, D.; Mishra, V.; Jomaa, M.; Liu, X.; Karmakar, A.; Thirupurasanthiran, S.; Michaelis, V. K.; Grosvenor, A. P.; Meldrum, A.; Mar, A. Controlling the Luminescence of Rare-Earth Chalcogenide Iodides $RE_3(Ge_{1-x}Si_x)_2S_8I$ (RE = La, Ce, and Pr) and $Ce_3Si_2(S_{1-y}Se_y)8I$. Chem. Mater. 2023, 35 (15), 6039–6049.
- (14) Zhou, W.; Yao, W.-D.; Zhang, Q.; Xue, H.; Guo, S.-P. Introduction of Li into Ag-Based Noncentrosymmetric Sulfides for High-Performance Infrared Nonlinear Optical Materials. *Inorg. Chem.* **2021**, *60* (7), 5198–5205.
- (15) Anand, A.; Zaffalon, M. L.; Cova, F.; Pinchetti, V.; Khan, A. H.; Carulli, F.; Brescia, R.; Meinardi, F.; Moreels, I.; Brovelli, S. Optical and Scintillation Properties of Record-Efficiency CdTe Nanoplatelets toward Radiation Detection Applications. *Nano Lett.* **2022**, 22 (22), 8900–8907.
- (16) Nikl, M.; Yoshikawa, A. Recent R&D Trends in Inorganic Single-Crystal Scintillator Materials for Radiation Detection. *Adv. Opt. Mater.* **2015**, 3 (4), 463–481.
- (17) Eijk, C. W. E. V. Inorganic Scintillators in Medical Imaging. *Phys. Med. Biol.* **2002**, *47* (8), R85–R106.
- (18) Touš, J.; Blažek, K.; Pína, L.; Sopko, B. High-Resolution Imaging of Biological and Other Objects with an X-Ray Digital Camera. *Appl. Radiat. Isot.* **2010**, *68* (4–5), *65*1–*653*.
- (19) Cao, F.; Yu, D.; Ma, W.; Xu, X.; Cai, B.; Yang, Y. M.; Liu, S.; He, L.; Ke, Y.; Lan, S.; Choy, K.-L.; Zeng, H. Shining Emitter in a Stable Host: Design of Halide Perovskite Scintillators for X-Ray Imaging from Commercial Concept. ACS Nano 2020, 14 (5), 5183–5193
- (20) Shao, Y.; Conner, R. L.; Souza, N. R. S.; Silva, R. S.; Jacobsohn, L. G. Fabrication of Ceramic Scintillators by Laser Sintering: The Case of Lu₃Al₅O₁₂:Pr. *Jpn. J. Appl. Phys.* **2023**, *62* (1), 010601.
- (21) Berseneva, A. A.; Masachchi, L. W.; Jacobsohn, L. G.; zur Loye, H.-C. Tunable Salt-Inclusion Chalcogenides for Ion Exchange, Photoluminescence, and Scintillation. *Chem. Mater.* **2023**, 35 (3), 1417–1431.
- (22) Van Haecke, J. E.; Smet, P. F.; Poelman, D. Luminescent Characterization of CaAl₂S₄:Eu Powder. *J. Lumin.* **2007**, *126* (2), 508–514.
- (23) Li, D.; Clark, B. L.; Keszler, D. A.; Keir, P.; Wager, J. F. Color Control in Sulfide Phosphors: Turning up the Light for Electroluminescent Displays. *Chem. Mater.* **2000**, *12* (2), 268–270.
- (24) Yang, L.; Li, Z.; He, L.; Sun, J.; Wang, J.; Wang, Y.; Li, M.; Zhu, Z.; Dai, X.; Hu, S.-X.; Zhai, F.; Yang, Q.; Tao, Y.; Chai, Z.; Wang, S.; Wang, Y. Emergence of a Lanthanide Chalcogenide as an Ideal Scintillator for a Flexible X-Ray Detector. *Angew. Chem., Int. Ed.* 2023, 62 (33), No. e202306465.
- (25) Lee, S.-P.; Huang, C.-H.; Chan, T.-S.; Chen, T.-M. New Ce³⁺-Activated Thiosilicate Phosphor for LED Lighting—Synthesis, Luminescence Studies, and Applications. *ACS Appl. Mater. Interfaces* **2014**, *6* (10), 7260–7267.
- (26) King, A. A.; Breton, L. S.; Morrison, G.; Smith, M. D.; zur Loye, H.-C. Boron Chalcogen Mixture Method-Assisted Alkali Halide Flux Crystal Growth of an Extensive Family of Quaternary Rare Earth Transition-Metal Thiosilicates: Investigation of Their Structures and Magnetic Properties. *Inorg. Chem.* **2023**, *62* (44), 18172–18178.
- (27) Breton, L. S.; Baumbach, R.; Tisdale, H. B.; zur Loye, H.-C. Structures and Magnetic Properties of $K_2Pd_4U_6S_{17}$, $K_2Pt_4U_6S_{17}$, Rb₂Pt₄U₆S₁₇, and Cs₂Pt₄U₆S₁₇ Synthesized Using the Boron-Chalcogen Mixture Method. *Inorg. Chem.* **2022**, *61* (27), 10502–10508.
- (28) Breton, L. S.; Klepov, V. V.; zur Loye, H.-C. Facile Oxide to Chalcogenide Conversion for Actinides Using the Boron-Chalcogen Mixture Method. *J. Am. Chem. Soc.* **2020**, *142* (33), 14365–14373.
- (29) Zhou, Y.; Iyer, A. K.; Oliynyk, A. O.; Heyberger, M.; Lin, Y.; Qiu, Y.; Mar, A. Quaternary Rare-Earth Sulfides $RE_3M_{0.5}M'S_7$ (M=Zn, Cd; M'=Si, Ge). J. Solid State Chem. **2019**, 278, 120914.

- (30) Usman, M.; Smith, M. D.; Morrison, G.; Klepov, V. V.; Zhang, W.; Halasyamani, P. S.; zur Loye, H.-C. Molten Alkali Halide Flux Growth of an Extensive Family of Noncentrosymmetric Rare Earth Sulfides: Structure and Magnetic and Optical (SHG) Properties. *Inorg. Chem.* **2019**, 58 (13), 8541–8550.
- (31) Daszkiewicz, M.; Marchuk, O. V.; Gulay, L. D.; Kaczorowski, D. Crystal Structures and Magnetic Properties of $R_2PbSi_2S_8$ (R = Y, Ce, Pr, Nd, Sm, Gd, Tb, Dy, Ho), $R_2PbSi_2Se_8$ (R = La, Ce, Pr, Nd, Sm, Gd) and $R_2PbGe_2S_8$ (R = Ce, Pr) Compounds. *J. Alloys Compd.* **2012**, *519*, 85–91.
- (32) Gitzendanner, R. L.; Spencer, C. M.; DiSalvo, F. J.; Pell, M. A.; Ibers, J. A. Synthesis and Structure of a New Quaternary Rare-Earth Sulfide, La₆MgGe₂S₁₄, and the Related Compound La₆MgSi₂S₁₄. *J. Solid State Chem.* **1997**, *131* (2), 399–404.
- (33) King, A. A.; Breton, L. S.; Morrison, G.; Smith, M. D.; Liang, M.; Halasyamani, P. S.; zur Loye, H.-C. Crystal Structures and Property Measurements of Rare Earth Magnesium Thiosilicates Synthesized via Flux Crystal Growth Utilizing the Boron Chalcogen Mixture (BCM) Method. *Inorg. Chem.* 2023, 62 (19), 7446–7452.
- (34) Lee, S.-P.; Chan, T.-S.; Chen, T.-M. Novel Reddish-Orange-Emitting BaLa₂Si₂S₈:Eu²⁺ Thiosilicate Phosphor for LED Lighting. *ACS Appl. Mater. Interfaces* **2015**, *7* (1), 40–44.
- (35) Krause, L.; Herbst-Irmer, R.; Sheldrick, G. M.; Stalke, D. Comparison of Silver and Molybdenum Microfocus X-Ray Sources for Single-Crystal Structure Determination. *J. Appl. Crystallogr.* **2015**, 48 (1), 3–10.
- (36) Sheldrick, G. M. SHELXT-Integrated Space-Group and Crystal-Structure Determination. *Acta Crystallogr. Sect. Found. Adv.* **2015**, *71* (1), 3–8.
- (37) Hübschle, C. B.; Sheldrick, G. M.; Dittrich, B. ShelXle: A Qt Graphical User Interface for SHELXL. *J. Appl. Crystallogr.* **2011**, 44 (6), 1281–1284.
- (38) Dolomanov, O. V.; Bourhis, L. J.; Gildea, R. J.; Howard, J. A.; Puschmann, H. OLEX2: A Complete Structure Solution, Refinement and Analysis Program. *J. Appl. Crystallogr.* **2009**, 42 (2), 339–341.
- (39) Spek, A. L. Single-Crystal Structure Validation with the Program PLATON. J. Appl. Crystallogr. 2003, 36 (1), 7–13.
- (40) Kubelka, P. Ein Beitrag Zur Optik Der Farbanstriche. Z. Tech Phys. 1931, 12, 593-601.
- (41) Daszkiewicz, M.; Gulay, L. D.; Lychmanyuk, O. S.; Pietraszko, A. Crystal Structure of the $R_3Ag_{1-\delta}SiS_7$ (R= La, Ce, Pr, Nd, Sm, Δ = 0.10–0.23) Compounds. *J. Alloys Compd.* **2008**, 460 (1–2), 201–205.
- (42) Kutahyali Aslani, C.; Breton, L. S.; Klepov, V. V.; Zur Loye, H.-C. A Series of $Rb_4Ln_2(P_2S_6)(PS_4)_2$ (Ln= La, Ce, Pr, Nd, Sm, Gd) Rare Earth Thiophosphates with Two Distinct Thiophosphate Units $[PVS_4]^{3-}$ and $[P\ IV_2S_6]^{4-}$. Dalton Trans. **2021**, 50 (5), 1683–1689.
- (43) Shi, Y.-F.; Chen, Y.; Chen, M.-C.; Wu, L.-M.; Lin, H.; Zhou, L.-J.; Chen, L. Strongest Second Harmonic Generation in the Polar R₃MTQ₇ Family: Atomic Distribution Induced Nonlinear Optical Cooperation. *Chem. Mater.* **2015**, *27* (5), 1876–1884.
- (44) Klepov, V. V.; Breton, L. S.; Pace, K. A.; Kocevski, V.; Besmann, T. M.; Zur Loye, H.-C. Size-Driven Stability of Lanthanide Thiophosphates Grown from an Iodide Flux. *Inorg. Chem.* **2019**, *58* (9), *6565–6573*.
- (45) Muenchausen, R. E.; Jacobsohn, L. G.; Bennett, B. L.; McKigney, E. A.; Smith, J. F.; Valdez, J. A.; Cooke, D. W. Effects of Tb Doping on the Photoluminescence of Y₂O₃:Tb Nanophosphors. *J. Lumin.* **2007**, *126* (2), 838–842.
- (46) Santos, J. C. A.; Silva, E. P.; Souza, N. R. S.; Alves, Y. G. S.; Sampaio, D. V.; Kucera, C.; Jacobsohn, L. G.; Ballato, J.; Silva, R. S. Laser Sintering and Photoluminescence Study of Tb-Doped Yttrium Aluminum Garnet Ceramics. *Ceram. Int.* **2019**, 45 (3), 3797–3802.
- (47) Morrison, G.; Latshaw, A. M.; Spagnuolo, N. R.; Zur Loye, H.-C. Observation of Intense X-Ray Scintillation in a Family of Mixed Anion Silicates, Cs₃RESi₄O₁₀F₂ (RE= Y, Eu-Lu), Obtained via an Enhanced Flux Crystal Growth Technique. *J. Am. Chem. Soc.* **2017**, 139 (41), 14743–14748.

- (48) Tarasenko, M. S.; Berezin, A. S.; Kiryakov, A. S.; Piryazev, D. A.; Filatova, I. Yu.; Naumov, N. G. Synthesis, Crystal Structure and Photoluminescence of Eu³⁺ or Tb³⁺ Doped Solid Solutions $(Y_{1-x}RE_x)_4S_3(Si_2O_7)$. J. Solid State Chem. **2018**, 265, 36–41.
- (49) Jia, D.; Meltzer, R. S.; Yen, W. M. Ce3+ Energy Levels Relative to the Band Structure in CaS: Evidence from Photoionization and Electron Trapping. *J. Lumin.* **2002**, *99* (1), 1–6.
- (50) Sharma, G.; Lochab, S. P.; Singh, N. Luminescence Properties of CaS:Ce, Sm Nanophosphors. *Phys. B Condens. Matter* **2011**, 406 (10), 2013–2017.
- (51) Pagonis, V.; Ankjærgaard, C.; Murray, A. S.; Jain, M.; Chen, R.; Lawless, J.; Greilich, S. Modelling the Thermal Quenching Mechanism in Quartz Based on Time-Resolved Optically Stimulated Luminescence. *J. Lumin.* **2010**, *130* (5), 902–909.